Contents lists available at ScienceDirect

Applied Surface Science

Full Length Article

Influence of roughness, porosity and grain morphology on the optical properties of ultrathin Ag films

Luca Ciambriello , Emanuele Cavaliere , Luca Gavioli [*]

Interdisciplinary Laboratories for Advanced Materials Physics (i-LAMP) and Dipartimento di Matematica e Fisica, Università Cattolica del Sacro Cuore, Via della Garzetta 48, 25133 Brescia, Italy

ARTICLE INFO

ABSTRACT

The dielectric function $\varepsilon(\omega)$ determines the optical behavior of thin and ultrathin metal films, crucial for many research areas and devices. Surprisingly, even for the paradigmatic case of evaporated Ag films, a large scattering of $\varepsilon(\omega)$ exists, mainly because the film is modelled by neglecting grain structure and surface roughness. Here, we quantitatively describe the optical - morphological relationships for Ag films in the 5.4 to 63 nm range thermally evaporated on fused silica. The experimental reflectance and transmission spectra are reproduced by a multilayer model employing an effective medium approximation for each layer. For the 9 nm thick film we describe how the film grain size and shape, porosity and surface roughness determine the reflectance and transmission spectra, and the total film $\varepsilon(\omega)$. Moreover, we provide the thickness dependent trend of the morphology-optical response correlation thus obtaining a complete quantitative description of the Ag films behavior up to the transition to the bulk regime. These results make this work a milestone in the morphology-optical understanding for ultrathin metal films and open new perspectives in the interpretation of thin film properties and in the design of the optical response of a tailored system.

1. Introduction

Thin and ultrathin films represent a potential and a challenge for many applications, such as plasmonic devices [1], photovoltaic cells [52], transparent conductive multilayers [3], electronics [5], sensor, [6,27] optical [1] and antimicrobial coatings [7–9]. In these systems, the interplay between the optical response and the morphological structure, *e.g.* grain size and shape, porosity and surface roughness, is greatly enhanced. Localized surface plasmon resonances (LSPR) are determined by the grain extension and crystallinity [1], which confines free electron motion, and by defects and film thickness [1,11–13,34]. The surface roughness of film acts in a similar way as a scattering interface for electron propagation, also influencing the electromagnetic and chemical enhancement of Raman scattering [14]. Moreover, the Stransky-Krastanov or Volmer-Weber growth mode of such systems results in the presence of voids or pores inside the film and a surface roughness comparable to the film height. Hence the distribution and shape of the voids gives rise to a non-trivial behavior of light/film interaction, making the determination of the optical constants – film morphology relationship complicated [10]. A recent review [1] indeed underlines

the large differences in the dielectric function $\varepsilon(\omega)$ determined from experimental data obtained on nominally similar Ag thin and ultrathin films deposited by thermal evaporation. The calculated $\varepsilon(\omega)$ of such paradigmatic systems, obtained on oxide or glass substrates, turns out to be strongly affected by deposition conditions [15,16] and by in-growth or subsequent substrate annealing treatments [17–19]. One of the basic and yet unresolved issues determining such reported data scattering [1,20] is due to the assumption of modelling the system with a single homogeneous and uniform bulk layer. In this framework the $\varepsilon(\omega)$, obtained by the numerical inversion of reflectance (R) and transmission (T) data, or of ψ and Δ coefficients in spectroscopic ellipsometry [21], completely neglects the grain structure and the surface roughness influence on the optical response [22,23]. Moreover, normal incidence R and T data are not sufficient to determine unambiguously the dielectric function [24], since different solutions are compatible with experimental data. Hence, further R or T data at other incidence angles [25] have to be included in the numerical inversion [13]. In other cases, an analytical expression for the film dielectric function is built up *ad hoc* by adding oscillators to match the calculated R and T [26] or ψ and Δ [12,27,28] with the measured ones.

A further issue stems from the presence of pores or voids in the film structure, which strongly influence the physical properties [29,30]. In such case, a mean field Bruggeman's effective medium approximation (BEMA) [31,32] is adopted to calculate the dielectric function. If the characteristic film grain size, void size and surface roughness are limited to 1/10 of the impinging light wavelength [33], the BEMA model is able to account for the shape of the inclusions through the depolarization factor q [36,45]. Since q describes the charge redistribution occurring in the volume and surface of the voids or grains subjected to the propagating electric field, this model is notably able to account for localized surface plasmon resonances (LSPR) without forcibly introducing external oscillator terms in the dielectric function of the material. However, for nanostructured materials a single BEMA layer may not be enough to properly describe the surface roughness and the gradients along the film depth, either in porosity or in grain size and shape. These effects can be accounted for only by modelling the sample as a multi-layer stack in which each layer is described by a proper EMA with suitable depolarization and void factor, as applied in similar the cases of AgTiO$_2$ thin films [35,36] or nanoporous gold [37].

The third issue raises when morphology data of the film are present but no quantitative relation with the optical spectra is established. For instance, the LSPR shape and position are qualitatively ascribed to the presence of Ag domains [16,38] with different densities and sizes [39–41]. For spheroidal inclusions each spectral resonance has been associated to a spheroid axis, while the redshift has been attributed to a grain deformation [38]. In [16] the LSPR frequency redshift is empirically related to the grain size increase measured by AFM.

Finally, if the extracted dielectric function is compared to the one calculated from an effective medium approximation (EMA) model [12,27] and the film grain shape and film porosity is estimated [42–44], surface roughness, morphology gradient, dependence of porosity and domain shape along the film depth are not considered. A two layer model is employed in [11], with a top roughness layer and a core Ag region. However, in this configuration the roughness thickness is determined, while no morphological insight is provided for the inner region, being not described by an EMA. Only one recent work included the surface roughness in the BEMA model to describe a Ag ultrathin film deposited on an aluminum oxide crystal, the film being however obtained by direct deposition of Ag grains, thus giving rise to a very different system with respect to a thermally evaporated Ag film [35].

To summarize, a complete and quantitative characterization of ultrathin thin Ag films to establish a precise relationship between morphological parameters and optical properties including porosity, grain shape, percolation and roughness, is still missing. In this work, we present the results for the paradigmatic case of ultrathin Ag films obtained by thermal evaporation on fused silica. The experimentally measured morphology and optical characteristics are quantitatively described by modelling reflectance and transmission spectra with a multi-layer BEMA configuration. The model, implemented through a new home-made code for ellipsometry, reflectance and transmission spectra computation and fitting (Determination of Effective Multilayer Optical constants for Nanotechnology – DEMON), provides fundamental physical insights on the morphology-optical correlation. In particular, the thickness and morphology dependence of the optical features is described in detail, highlighting the role of the film roughness and the presence of voids in the determination of the dielectric function of the films.

2. Materials and methods, calculation

The Ag films have been deposited on 1 mm thick silica (SiO_2) substrates (MaTeck GmbH Germany) at room temperature in medium vacuum (base pressure = 1x10^{-6} mbar), employing 99.999% purity Ag in a home-made thermal evaporator placed at 20 cm from the substrate, with typical deposition rate of 3 nm/min. Films heights range from 5 nm to 63 nm, as measured from the film/substrate edge by atomic force

microscopy (AFM) (Park NX10) in both non-contact and tapping mode using a PPP-NCHR tip (resonance frequency in the 250–280 kHz range, nominal tip radius 10 nm) by nanosensor. The rooot mean square (RMS) roughness has been obtained using the Gwyddion software from AFM data on different 1x1 μm^2 images acquired with a 512x512 square pixels size. Transmission (T) and reflectance (R) spectra in the 250 nm – 1500 nm range have been measured in air at normal and 7° incidence angle, respectively, by a Perkin-Elmer Lambda950 spectrophotometer equipped with an integrating sphere.

The new home-made fitting and computation software DEMON has been written in Python and implemented to analyze optical spectra. A detailed description of the code can be found in the supplementary information (S.1). Any experimental film is modelled by a stack of an arbitrary number of layers, assuming the light incident from the top at an incidence angle which can be chosen arbitrarily, as depicted in Fig. 1a, and assuming a wavelength 10 times larger than the inclusion size [33].

Each layer is described by its own dielectric function $\varepsilon_L(\omega) = \varepsilon_{1L}(\omega) + i\varepsilon_{2L}(\omega)$ or, equivalently, by a refractive index $N_L(\omega) = n_L(\omega) + ik_L(\omega) = \sqrt{\varepsilon_L(\omega)}$. If a layer is not homogeneous in composition or morphology, ϵ becomes an effective dielectric function deriving from an appropriate EMA. In the present case we have adopted a BEMA model. If the material composing the layer consists of n elements, the effective dielectric function ϵ can be identified as the solution of the Bruggeman's equation:

$$\sum_{i=1}^{n} f_{(i)} \frac{\varepsilon_{(i)} - \varepsilon_L}{\varepsilon_L + q(\varepsilon_{(i)} - \varepsilon_L)} = 0 \tag{1}$$

where $\varepsilon_{(i)}$ are the dielectric functions of each of the composites, q is the depolarization factor describing the shape of the inclusions and $f_{(i)}$ are the volume fractions of each composite. Clearly $\sum_i f_{(i)} = 1$. q , varying in the range $0 \leq q \leq 1$, depends on the shape and the orientation of the inclusions with respect to the incident electric field [45]. For $q = 0$ the inclusions assume the shape of a plane parallel to the incident electric fields (Fig. 2a); for $q = 1/3$ the inclusions are modelled as spheres (Fig. 2b); for $q = 1$ the inclusions are pillar-like structures with the longer side normal to the electric field (Fig. 2c).

To reproduce the porosity of a layer it is sufficient to attribute one of the inclusions in eq. (1) to the pore's vacuum ($\varepsilon_{(i)} = \varepsilon_{(v)} = 1$) , hence we refer to $f_{(i)} = f_{(v)}$ as the porosity. In this framework, the f and q EMA parameters describe the layer morphology, while the possibility of stacking multiple layers accounts for a morphology gradient, allowing to select for each layer the same bulk $\epsilon^{(i)}$ but different q and f values in each Bruggeman's EMA (eq. (1)). In particular, the film roughness is modelled by a top layer with a fixed 50% void factor in the EMA, i.e. $f_{(v)} = 0.5$. The DEMON software allows to fit the experimental R and T intensities (or as an option the ψ and Δ ellipsometry data), by means of the transfer matrix method, within any multi-layer and EMA configurations assumed for the model. An in-depth validation of the routine on previously published results obtained on gold films has been described in detailed in the supplementary information (S.2). In this work we have analyzed the R and T optical spectra acquired at normal incidence. The fitting routine minimizes the quantity:

$$\left(R_{exp} - R_{calc}\right)^2 + \left(T_{exp} - T_{calc}\right)^2 \tag{2}$$

where, "exp" indicates measured quantities and "calc" the computation outputs. The fit has been considered to converge if the deviation of both calculated R and T from the experimental values do not exceed 2% in the entire spectrum, while the uncertainty on the fitting parameters corresponds to a 4% standard deviation. In the case of thermally evaporated Ag films the multi-layer configuration is schematically reported in Fig. 1(b): starting from the bottom, a 1 mm thick fused silica substrate is followed by one or two core Ag layers, ending the stack with a roughness layer. The pure Ag dielectric function is expressed as a
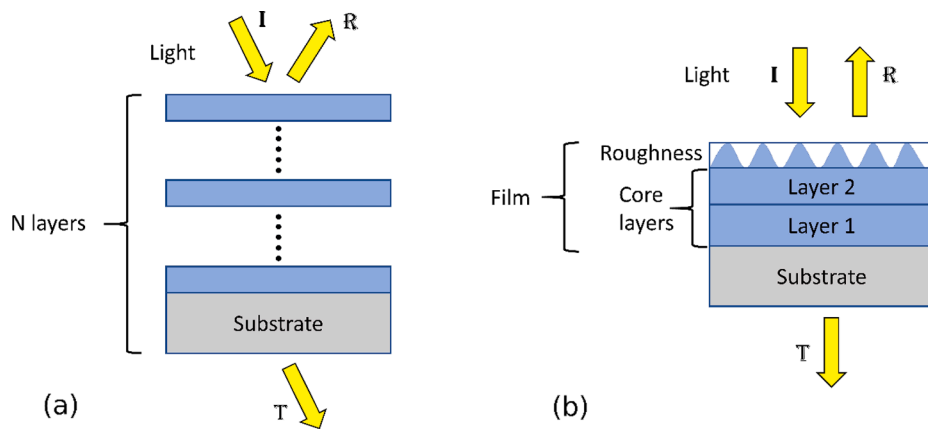
Fig. 1. (a) General configuration of a stacked multilayer model that can be used in the home made DEMON code. Each layer has its own dielectric function that can be modeled by a BEMA. Furthermore, the top layer may represent the film surface roughness if the void filling fraction is set to 50%. (b) The configuration adopted in this work to reproduce the Ag ultrathin films: on the 1 mm thick silica substrate, either one or two core layers are considered and each layer is modelled with its own BEMA. In the top layer film the porosity is fixed to 50% to reproduce the film roughness.
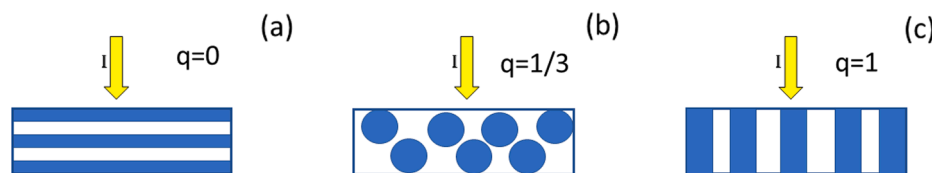

Fig. 2. Geometry dependence of the Inclusion shapes associated to different depolarization factors q for the case of normal incidence light. (a) For q = 0 the inclusions have a sheet shape and the plane is parallel to the incident electric field. (b) For q = 1/3 the inclusions assume a spherical shape. (c) For q = 1, the inclusions become pillar-like with the longer side normal to the incident electric field.

function of the photon angular frequency ω :

$$\varepsilon_{Ag}(\omega) = \varepsilon_{\infty} + \varepsilon_{IB}(\omega) - \frac{\omega_{pl}^2}{\omega^2 + i\Gamma\omega} \quad (3)$$

Here, ε_{∞} is the constant dielectric background, which accounts for all the contribution from oscillators centered at energy scales far out of the investigation range. The second term ε_{IB} is the interband contribution, while the third term is the Drude oscillator, with a plasma frequency ω_{pl} and a scattering rate Γ. In the present work, the only fit parameter in the eq. (3) has been Γ, while all the other ones have been kept fixed and equal to the pure bulk Ag ones, reported in the supplementary information (S.3). The deviation of Γ from the bulk reference value may be

included by considering the electron scattering with the inclusion boundaries, hence quantifying the size of metal inclusions through:

$$\Gamma = \Gamma_{bulk} + \frac{A}{r}v_F \quad (4)$$

where v_F is the Fermi velocity and r is the inclusion radius [35,37,46,47]. A is a factor of the order of unity which depends on the inclusion shape [48]. Eq. (4), which directly relates one of the film morphological characteristics with the optical response, has been discussed through several models, leading to values for A around unity, with a dispersion of the order of 20% for the same given inclusion shape [49–51]. In the following $A = 1$ will be assumed. The silver dielectric
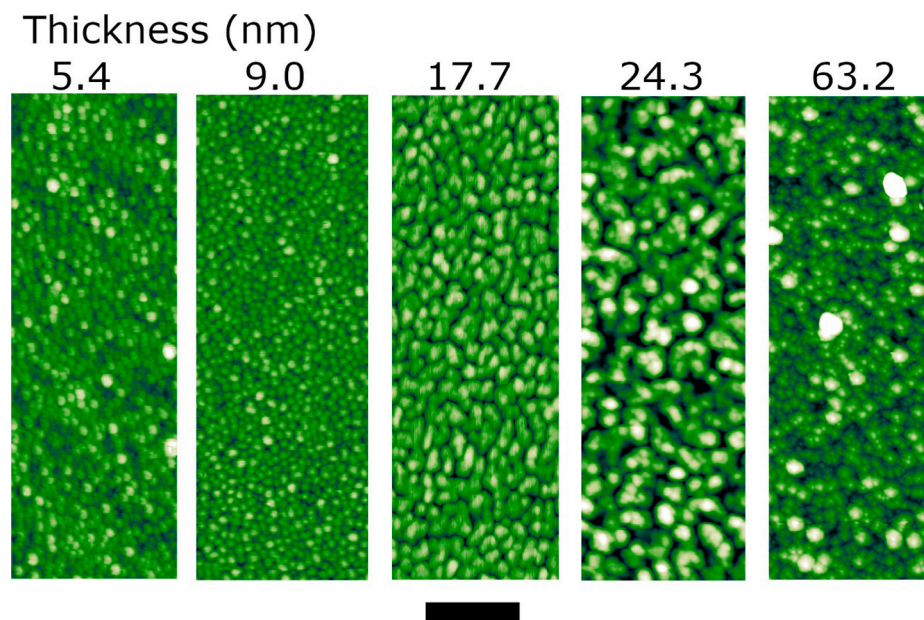

Fig. 3. *(0.25 × 1 μm²) AFM data on selected films. Scale bar 200 nm.*

function of eq. (3) has then be combined with the $\varepsilon = 1$ vacuum dielectric function within the BEMA described by eq. (1) with $n = 2$, to obtain the effective dielectric function of each layer.

3. Results and discussion

The data have been acquired and analyzed for nine different Ag films, with thicknesses from 5 nm to 63 nm. However, for the sake of clarity we present here the AFM images and the optical spectra for five films only to outline the trend of the physical and morphological features as a function of the film thickness. Fig. 3 shows the morphology of the selected films obtained by AFM. For 5 and 9 nm thickness, the films are constituted by well separated grains. From 17.7 to 24.3 nm thickness, one observes the formation of much larger wormlike structures, still clearly separated, while at higher coverage a more compact distribution of the surface structures is observed. The AFM data, quantified in Fig. 9 (f) by the measured roughness, clearly indicate that the morphology of such systems is far from being bulk-like and should be taken into account for a correct evaluation of the optical properties.

The insights on the optical-morphological properties relationships are obtained through the application of the multilayer model previously described (see Fig. 1b) to fit the R and T data. The number of layers describing the different films, including the top roughness layer, is two up to 9.0 nm and three for all other films (see Table 1). This choice allows to keep the number of layers as small as possible, supposing that the bottom layer in contact with the silica substrate is not affected by the

Table 1
Summary of the fit results for five selected Ag films, corresponding to the curves reported in Fig. 8. t is the layer thickness, $f_{(v)}$ the porosity and q the depolarization factor. For each film thickness data are organized in four columns, following the configuration sketched in Fig. 1b. The first column identifies the parameter, the second column provides the values for the core layer in contact with the substrate, the third column contains the parameters of the second core layer while the fourth presents the results for the top roughness layer. For the thickest film, the core layer 1 is beyond the light penetration hence its parameters are assumed in analogy to the other samples and labelled with an *. N.R.: not relevant with respect to the fitting results. The complete results are reported in table (S.4) of the supplementary information.

Film thickness (nm)	Parameter	Core layer 1	Core layer 2	Roughness layer
5.4	t (nm)	1.7 ± 0.4	–	3 ± 2
	$f_{(v)}$ (%)	12.7 ± 0.7	–	50
	q	0.996 ± 0.003	–	0.8 ± 0.1
	$\hbar\Gamma$ (eV)	0.4 ± 0.1	–	N.R.
9.0	t (nm)	3.9 ± 0.5	–	4 ± 2
	$f_{(v)}$ (%)	10.2 ± 0.5	–	50
	q	0.996 ± 0.003	–	0.70 ± 0.05
	$\hbar\Gamma$ (eV)	0.4 ± 0.1	–	N.R.
17.7	t (nm)	6 ± 1	8 ± 1	4 ± 2
	$f_{(v)}$ (%)	2.6 ± 0.4	0.9 ± 0.6	50
	q	0.992 ± 0.003	0.95 ± 0.02	0.6 ± 0.1
	$\hbar\Gamma$ (eV)	0.4 ± 0.2	0.2 ± 0.1	N.R.
24.3	t (nm)	5 ± 1	15 ± 1	3 ± 2
	$f_{(v)}$ (%)	3 ± 1	0.3 ± 0.2	50
	q	0.990 ± 0.008	0.983 ± 0.005	0.6 ± 0.2
	$\hbar\Gamma$ (eV)	0.4 ± 0.2	0.2 ± 0.1	N.R.
63.2	t (nm)	4*	55 ± 5	4 ± 2
	$f_{(v)}$ (%)	< 5*	0	50
	q	0.995*	–	0.82 ± 0.04
	$\hbar\Gamma$ (eV)	0.4*	0.02 (≤ 0.08)	N.R.

growth of the Ag films on top of it. The free fitting parameters for each of the layer are: 1) the scattering rate Γ ; 2) the individual layer thickness t ; 3) the porosity $f_{(v)}$; and the depolarization factor q . The general criterion is to maintain the fitting parameters values as constant as possible to fit the data when moving from one film to the next.

3.1. Optical - morphology features correlation

To outline the important features of R and T data and the role of each fitting parameter with respect to the physical response of the film, we discuss first the results obtained on the 9 nm and 63.4 nm thick systems. Fig. 4 reports the experimental R and T spectra (open dots) for the 9 nm film together with the best fitting curves obtained from the model. Below 330 nm, one can note a sharp minimum followed by a steep increase in the R spectrum and a sharp maximum in the T spectrum. Above 330 nm, the R data present a small shoulder in the 350–400 nm interval, followed by a broad peak centered at 500 nm and by a smooth intensity decrease in the infrared region. Conversely, the transmission data are characterized by a shoulder at 400 nm and a deep minimum at 500 nm, reaching a 90 % transmission above 800 nm.

The optical model employed for this particular film height consists of two Ag layers (a core layer in contact with the substrate and a roughness layer, see the scheme reported in Fig. 1(b)) on top of the 1 mm thick fused silica substrate. For the BEMA of each layer a dielectric function as described in eq. (3) has been used as input, where ε_∞ , ε_{IB} and ω_{pl} are the bulk values derived from the experimentally measured Ag metal refractive index in [23] (more details in the supplementary information S.3). The results from the R and T data fitting shown as blue lines in Fig. 4 provides for the core layer a 4.5 nm height with porosity $f_{(v)} = 10.2\%$ and depolarization $q = 0.996$, and for the top roughness layer a 4 nm height with $f_{(v)} = 50\%$ and $q = 0.7$. In the core layer the scattering rate is $\hbar\Gamma = 0.4$ eV providing a grain size of 2.4 nm through eq. (4), while in the roughness layer the optical response is not significantly affected ($<2\%$ variation in the R and T data) by $\hbar\Gamma$ for values in the range $0 eV \leq \hbar\Gamma < 1.5 eV$. The two features below 330 nm are completely reproduced in the fitting model by the presence of ϵ_{IB} , which stems from the interband transitions of bulk Ag. The other spectra characteristics are reproduced thanks to the film porosity, the depolarization factor and the scattering time included in the EMA model (see eq. (4)). q and Γ are related to the shape and size of grains inside the film, determining the morphology-dependent behavior of the LSPR resonance peaks. In our model, each resonance originates from an EMA as described in eq. (1)) and therefore one expects that the peak shape and position will depend on $f_{(v)}$, q and Γ .

We indeed now discuss the influence of the fitting parameters on the spectral characteristics of the optical data for the representative case of the 9 nm thick film to clarify the physical feature of the model. Fig. 5 presents the dependence of the calculated R and T spectra as a function of these three important parameter of the BEMA model, together with the experimental data. The influence of the layer porosity $f_{(v)}$ on the calculated optical response is shown in Fig. 5(a) and 5 (b). The main peak centered at 500 nm for both R and T is significantly blue-shifted by increasing $f_{(v)}$ from 10.2 % to 13% (blue curve), while it is red-shifted when $f_{(v)}$ is lowered to 7%, i.e. the overall trend is a blue shift of the LSPR peak related to an increasing layer void factor. The depolarization factor q has also a major impact on the LSPR peak since it affects the amplitude, the width and the wavelength position (see Fig. 5(c) and 5 (d)). By increasing q from 0.996 to 1, i.e. to a pillar like film morphology (see the scheme in Fig. 2(c)), the calculated R and T curves change from the black to the blue ones. The 510 nm peak shape becomes sharper, the amplitude increases and the wavelength is blue-shifted. On the other hand a decrease of q results in a R and T curves modification from the black to the red ones, in which we observe a larger peak width, an amplitude decrease and a red shift. Hence a small layer morphology modification from a complete pillar like arrangement determines a red
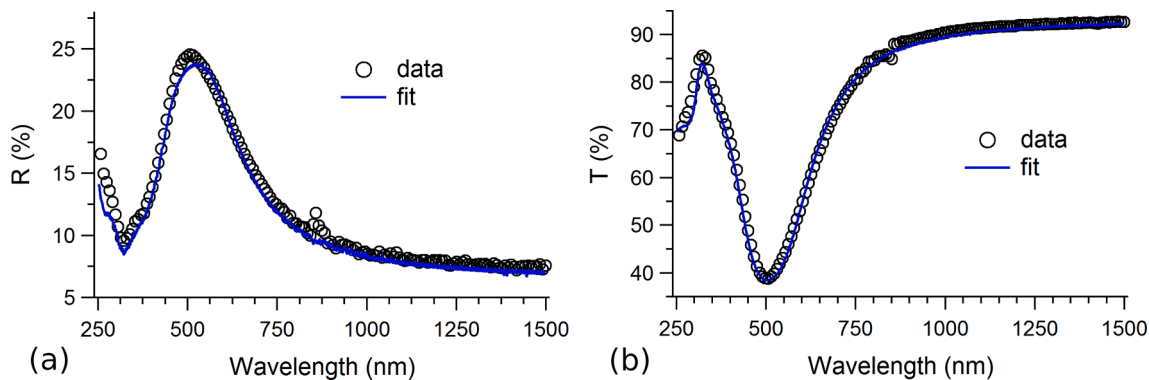
Fig. 4. Experimental data (open circles) of reflectance (a) and transmission (b), respectively, taken on a 9 nm thick Ag film deposited on a silica substrate. The blue lines represent the best fit obtained with the model described in the text.
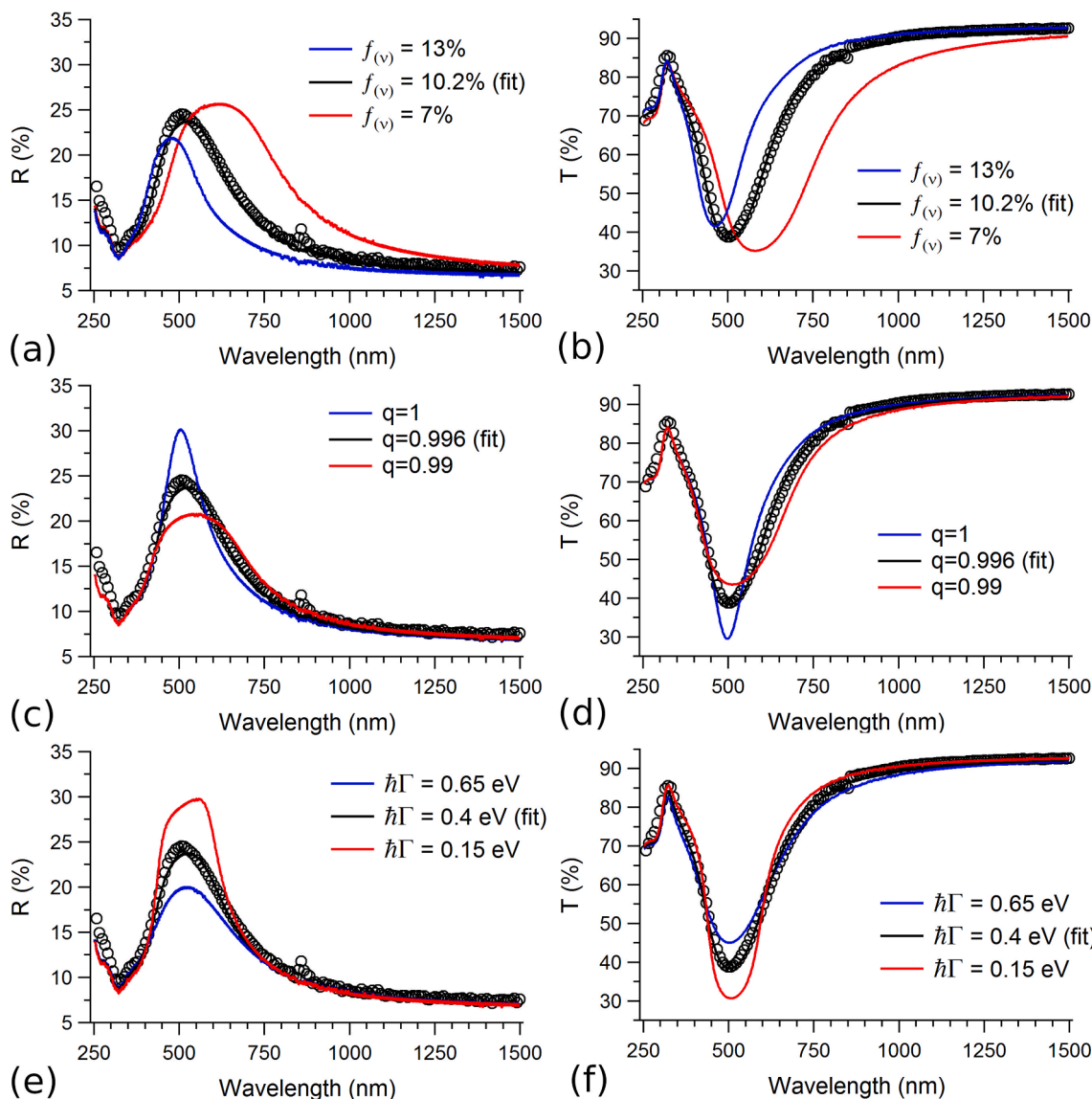

Fig. 5. Influence of the porosity (panels (a) and (b)), depolarization factor (panels (c) and (d)) and scattering rate (panels (e) and (f)) on the R and T spectral features for the case of 9 nm thick film. The black lines represent the best fit.

shift and a width increase of the LSPR.

Finally, the scattering rate Γ of the Drude oscillator affects mainly the peak amplitude as shown in Fig. 5 (e) and 5 (f), while the impact on the

peak width is limited. A 60% increase of Γ (from the black to the blue curve) corresponds to a 20% decrease of the peak intensity, as well as a decrease by 60% (from the black to the red curve) brings a 25% increase

of the peak intensity. Since the scattering rate is inversely proportional to the inclusion radius as shown in eq. (4)), the presented behavior indicates that LSPR amplitude is increasing when the grain size is decreasing.

The BEMA employed in top roughness layer is also very important since it allows to reproduce the shoulder located around 360 nm. For the 9 nm film the effect is barely evident, being overwhelmed by the main peak, but its effect becomes clear for thicker films as shown in Fig. 6 for the 63.4 nm case. For wavelengths higher than 500 nm the R and T spectra are almost flat, while a shoulder in the 350 to 450 nm range is visible in the R spectrum. The black curve results from the data fitting for a film modelled by a three-layers stacking, as described in detailed below, in which the central core layer is bulk-like and homogeneous and the top layer describes the film roughness, with $f_{(v)} = 50\%$ and $q = 0.82$. The fit is well reproducing the experimental data throughout the entire wavelength range for both R and T. In Fig. 6 we also report the fitting results for a model configuration without the top roughness layer (blue curve). It clear that such case cannot reproduce the experimental data, in particular the reflectance in the 280–450 nm range, while it does not significantly differ for the transmission. The discrepancy can be accounted for only when the roughness layer is included. This clearly indicate that even for a 63 nm thick Ag film a roughness layer of 4 nm must be considered to justify the experimental data up to 500 nm wavelength, also clearly indicating that the bulk layer determines the optical behavior above 500 nm.

To underline the importance of appropriately considering the system morphology by modelling the film with a multilayer stack, we report in Fig. 7 the real (ε_1) and imaginary (ε_2) parts of the effective dielectric functions of the top roughness layer (red line) and the core layer (blue line) for the 9 nm film case. The imaginary part ε_2 tends to zero for wavelengths above 1000 nm in both layers, indicating a vanishing infrared absorption. In the same region of the spectrum, the real part ε_1 shows small variations, resulting in a limited excursion in R and T spectra. In the 350–800 nm range, the core layer is characterized by a marked peak in ε_2 at 500 nm accompanied by a zero of ε_1, implying an absorption structure and giving rise to the LSPR peaks found in the R and T spectra. We remark how the resonance centered at 500 nm wavelength is produced directly from the core layer BEMA without introducing other oscillators in the dielectric functions. The roughness layer is characterized by a much lower and broader ε_2 peak and a more limited ε_1 excursion with respect to the core layer. The fact that the is positive is related to the combination of the metal Ag dielectric function with the vacuum dielectric function inside the Bruggeman equation. The effective dielectric functions obtained for the two layers can also be combined to give the overall film ε (Fig. 6, black lines). For this purpose, each individual layer ε is summed by using a BEMA with $q = 0$ (this value corresponds to the parallel layers configuration as in Fig. 2a) to reproduce the stacking of the two layers. In this case the total dielectric

function results as an average of the two layer's dielectric functions weighted by their thicknesses. As showed in Fig. 7, the total ε shape is mainly determined by the core layer contribution, while the roughness layer act as a damper of the feature intensities. It is clear that the possibility to describe the overall film behavior through a multilayer model provides the physical insights on the optical-morphology correlation. Furthermore, this approach is also very flexible and could be easily adapted to other types of ultrathin films in which the composition and morphology may be more complicated.

To summarize, the presented results establish a direct quantitative connection between experimental R and T data and important morphological information such as porosity, inclusion size and shape, and film roughness. For each layer the $f_{(v)}$, q and Γ BEMA parameters can be determined by the shape and position of the resonances occurring in spectra.

3.2. Thickness dependence of the morphology-optical properties correlations

We now discuss the relationships among the model parameters and the physical quantities as a function of the film thickness. Fig. 8 (a) and (b) show the reflectance and transmission experimental data (open circles) and the fit results (lines) for selected film heights, as well as the absorption (A) in Fig. 8 (c), obtained as A = 100%-R-T. The reflectance behavior (Fig. 8a) is characterized by a small peak centered around 460 nm for the 5.4 nm film, increasing in intensity and shifting to 500 nm for the 9.0 nm thick film. The R intensity is then increasing for thicker films, in particular in the infrared region, to reach an almost flat plateau above 500 nm for the 63.2 nm film. The transmission is characterized by a marked dip centered at 470 nm for the thinnest film, shifting to 500 nm and broadening for the 9.0 nm thick film. The spectrum shape is then strongly modified above 550 nm for the 17.7 nm, becoming sharply peaked at 320 nm for the 63.2 nm film. The resulting absorption curves present a distinct peak centered at 460 nm, accompanied by a shoulder around 360 nm for the 5.4 nm film. By increasing the film thickness to 9.0 nm the absorption peak shifts to 500 nm increasing its intensity. A major spectrum modification is observed at 17.7 nm thick film, characterized by an intense absorption (up to 40%) above 500 nm. Such behavior is further modified for the 24.3 nm film, since the overall absorption intensity above 500 nm starts to decrease. Reaching a constant 2 % value for the 63.4 nm film, characterized by the absorption structure below 470 nm.

The fitting of the thickness-dependent R and T data through the application of the multilayer model (see Fig. 1b) provides the insights on the optical-morphological properties relationships. The number of layers describing the different films, including the top roughness layer, has been limited to two up to 9.0 nm and to three for all other films (see Table 1), while the free fitting parameters for each of the layer are: 1) the
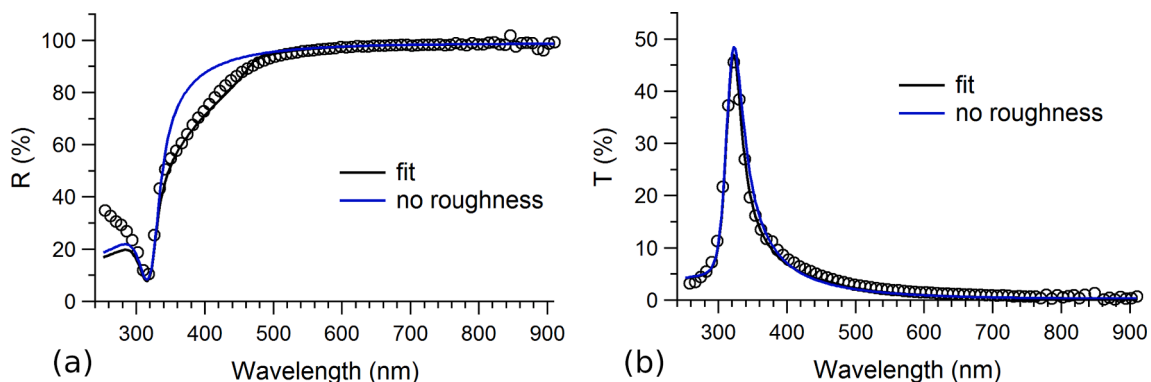

Fig. 6. R and T experimental spectra (dots) and fit curves (black lines) of the 63.4 nm film in the 250 nm – 700 nm range. The blue lines are the simulation for a model of the same thickness but without a roughness top layer.
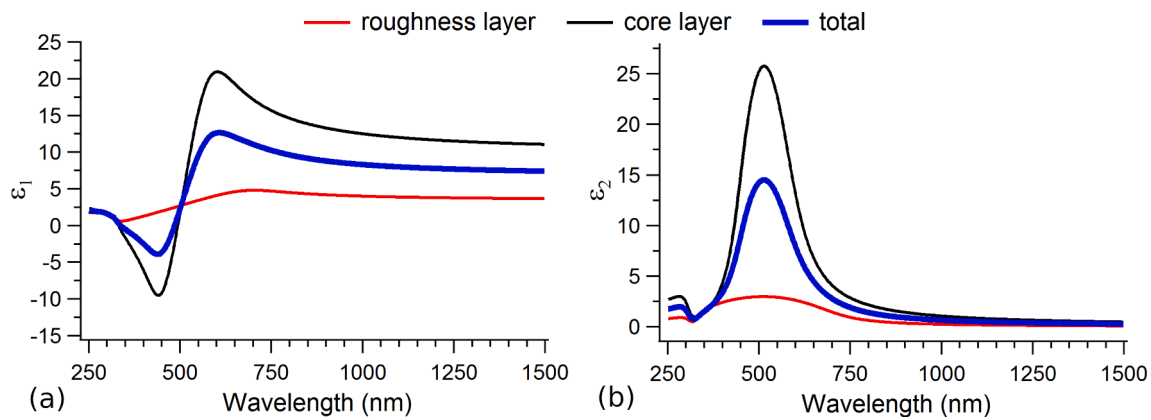
Fig. 7. Real ε_1 (a) and imaginary ε_2 (b) part of the dielectric functions of the top roughness layer (red line) and the core layer (blue line) for the 9 nm film model. The black line is the total dielectric function of the film calculated by combining the top and core dielectric functions through a BEMA with q = 0.
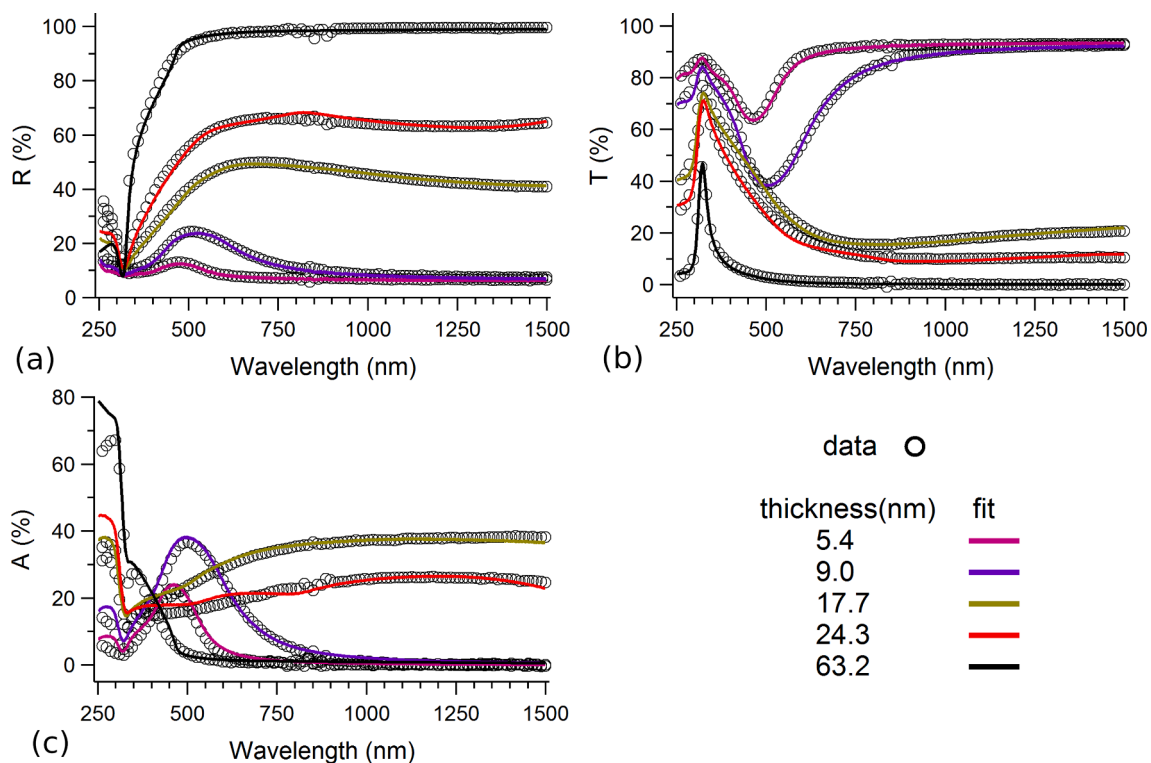

Fig. 8. R (panel a) and T (panel b) of five thermally evaporated silver films: dots are the measured values, while solid lines are the fitting outputs. Panel c shows absorption spectra obtained as A = 1-R-T. In panel c is also shown a simulated absorption (broken line) of a 9 nm bulk silver film.

scattering rate Γ ; 2) the individual layer thickness t ; 3) the porosity $f_{(v)}$; and the depolarization factor q . The general criterion is to maintain the fitting parameters values as constant as possible to fit the data when moving from one film to the next. The initial parameter values have been selected taking into account the film roughness and height measured by AFM.

The calculated R and T curves are shown for the selected films in Fig. 8 as straight lines, while the corresponding values of the fitting parameters are reported in Table 1. The R and T data and the fitting results for all the investigated films are presented in the supplementary information (Figure S.7 and table S.4). The transmission, reflectance and absorption curves obtained from the fitting model are in very good agreement with the data.

The thickness dependent trends of the relevant physical parameters are summarized in Fig. 9 and reported in detail in Table 1 and Table S4 of the supplementary information. The porosity $f_{(v)1}$ of the bottom layer

(Fig. 9(a)), in contact with the substrate, is decreasing from 13% to 3 % at 24.7 nm, while the porosity $f_{(v)2}$ of the core layer (appearing only from a film height of 13.5 nm) rapidly decrease from 5% to reach an almost bulk-like value at 24.3 nm. The depolarization factor (Fig. 9(b)) q_1 is varying only by 1% in the entire thickness range, indicating a pillar-like structure of the film/substrate interface layer, while the depolarization factor q_2 shows a dip at the intermediate coverages. Note that for the film/substrate interface layer, both $\hbar\Gamma_1$ (giving a grain size of 2.4 nm) and the thickness t_1 (Fig. 9(d) and 9 (e), respectively) are basically un-modified for all the thicknesses, suggesting that this is little affected by the film growth. On the other hand, $\hbar\Gamma_2$ of the core layer (and the layer height t_2) is decreasing (increasing) as a function of the increasing film thickness. This corresponds to an increase of the grain size up to 5.2 nm (Fig. 9(d)). The roughness layer height shown in Fig. 9 f) is in rather good agreement with the experimentally measured RMS roughness.

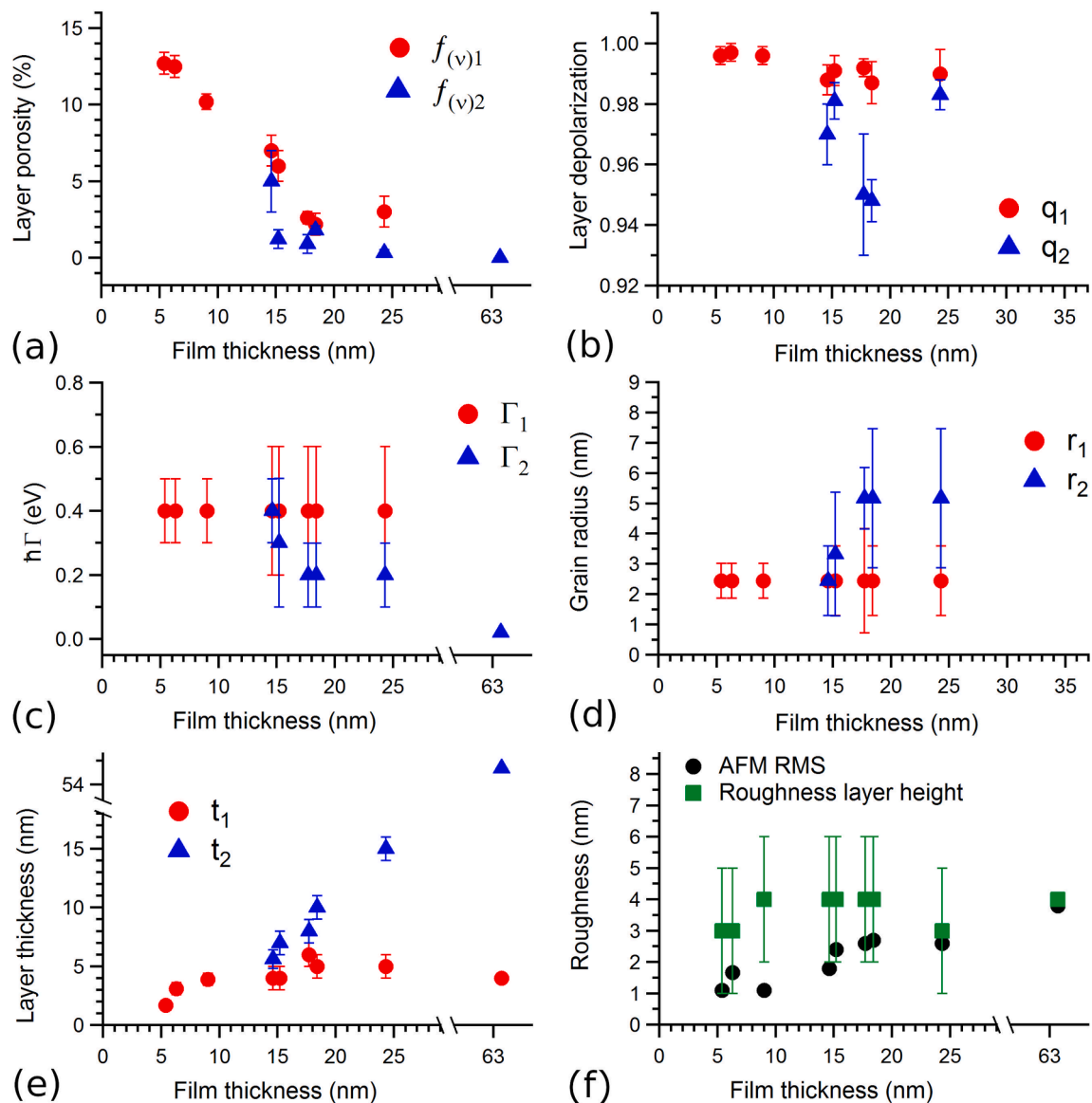The presented results establish a clear morphology – optical prop-

Fig. 9. The panels (a) to (d) present the thickness dependence of the porosity (a), depolarization factor (b), scattering time (c) and radius (d), respectively, of the first bottom (red dots) and second (blue triangles) layers employed in the model. Panel (e) reports the height of the layers employed for the different film thicknesses and panel (f) compares the film roughness (black dots) with the top roughness layer height employed in the model.

erties relation as a function of the film thickness and explain the origin of the optical features observed in the spectra. Below 330 nm wavelength the R and T spectra are dominated by the Ag interband transitions, whose intensity variation is explained simply by the increased film thickness. In the 330 – 900 nm region, the features are strongly thickness dependent. In the present model, describing each film up to 9 nm height by a single core layer plus a roughness layer, the main LSPR (the broad peak around 500 nm) emerges from the BEMA adopted in the core layer, that directly connects the peak shape and wavelength position to the layer porosity $f_{(v)}$ and to the Ag inclusions structure. The core layer is organized in pillar-like structures (q_1 close to 1, Fig. 9 (b)) with a grain size of 2.4 nm (Fig. 9 (d)). The LSPR redshift is accounted for by the porosity decrease ($f_{(v)1}$ in Fig. 9 (a)), the unchanged peak shape indicates a constant Ag inclusions structure, and the peak intensity variation is completely reproduced by an increase of the core layer thickness (t_1 from 1.8 nm to 4.5 nm, Fig. 9 (e)). The further although less evident LSPR around 360 is reproduced by the BEMA of the top roughness layer (with porosity set to $f_{(v)} = 50\%$). Above 900 nm wavelength plasmonic oscillations do not affect the spectra behavior, typical of the underlying

substrate. These results are in good agreement with the formation of grains in the growing film following the Volmer-Weber growth mode.

Above 9 nm, the much broader and asymmetric resonance extending in all the visible-infrared region (Fig. 7) requires the introduction of a second core layer, as detailed in the supplementary information (S.6). The elbow around 650 nm is deriving from the first core layer keeping constant thickness, q_1 and Γ_1 and a decreasing porosity justifying the redshift. The featureless part of the spectra above 650 nm is then accounted for by a resonance appearing in the BEMA of the second core layer. The lower depolarization factor q_2 determines the large resonance width and the lower porosity $f_{(v)2}$ with respect to the underlying first core layer explaining the position in the infrared region. In terms of film growth, the second core layer is schematized by grains growing on top of the first core layer, with a lower porosity, a grain size increasing up to 4.6 nm radius and shape converging to that of the first layer. At 24.3 nm film thickness, $f_{(v)2}$ approaches the bulk value (0%) and Γ_2 decreases, suggesting a formation of connected Ag domains larger with respect to the first core layer. For the 63.4 nm film the presence of a core layer 1 is no more effective since the light penetration length is lower than t_2.

Furthermore, the core layer 2 optical response is compatible with that of a bulk Ag metal. The only deviation from a perfectly homogeneous thin film is determined by the shoulder at 360 nm accounted for by the top roughness layer as discussed in paragraph 2.1. To summarize, the results provide fundamental insights on the influence of roughness, porosity and grain characteristics on R and T for thin Ag films.

The results presented may find a direct application in fields employing thin Ag films, *e.g.* plasmonic devices [28] or transparent conductive multilayers [3]. The correlation of the Ag ultrathin dielectric function with the grain size and roughness would allow to explain the data reported by *e.g.* ref. [28] and describe the plasmonic behavior in relation to the film morphology without arbitrary oscillators. The application of the present results to the data obtained for the Ag films presented in ref. [3] could explain the transmission and reflection response as a function of the aluminum zinc oxide (AZO) roughness, the possible presence of voids in the Ag film and the effect of the top coating AZO layers on the Ag film morphology. Such work would also allow to guide a further improvement of the transmission of the conductive layer by simulating the response of the sandwiched structure and determining the optimal roughness, grains size and thickness parameters required for the actual system growth. Finally, it is worth noting that the results presented in this work are easily transferable to any type of optical system that can be modelled with a stacked multilayer configuration. For example, multicomponent systems where two or more materials are present can be described through appropriate EMA, while gradients on the composition can be accounted for by employing multiple layers. Moreover, the DEMON code can be employed to physically explain data obtained from spectroscopic ellipsometry (as shown in section S5 of the supplementary information) in addition to UV–VIS spectrophotometry. The code may also be used to predict the R and T response and the dielectric function of a custom-devised system, thus providing a powerful tool for devising an optical system with the desired features, avoiding a trial and error approach.

4. Conclusions

In this work we presented a quantitative optical and morphological characterization of ultrathin thin Ag films in the 5.4–63 nm range deposited by thermal evaporation on fused silica. By exploiting a new home-made code (DEMON), we reproduce the reflectance and transmission data by modelling each film with a stacked multilayer geometry. The code calculates the dielectric function of each layer through the BEMA and the model describes the overall film morphology. We showed the influence of roughness, porosity, grain radius and shape on the R and T spectra in the 250–1500 nm wavelength range, obtaining the effective dielectric function of a 9 nm thick film. Moreover, we show the thickness dependence of the relevant physical quantities providing a complete description of Ag films behavior up to the transition to the bulk regime. These results establish a milestone in the understanding of the Ag ultrathin films and open new perspectives in the interpretation of thin film properties and in the design of the optical response of a tailored system.

CRediT authorship contribution statement

Luca Ciambriello: Methodology, Software, Validation, Investigation, Writing – original draft. **Emanuele Cavaliere:** Methodology, Validation, Investigation, Writing – original draft. **Luca Gavioli:** Conceptualization, Methodology, Validation, Writing – original draft, Funding acquisition.

Declaration of Competing Interest

The authors declare that they have no known competing financial interests or personal relationships that could have appeared to influence the work reported in this paper.

Acknowledgements

Appendix A. Supplementary data

Supplementary data to this article can be found online at https://doi.org/10.1016/j.apsusc.2021.151885.

References

[1] A.S. Baburin, A.M. Merzlikin, A.V. Baryshev, I.A. Ryzhikov, Y.V. Panfilov, I. A. Rodionov, Silver-based plasmonics: golden material platform and application challenges [Invited], Opt. Mater. Express. 9 (2) (2019) 611, https://doi.org/10.1364/OME.9.000611.

[3] G. Torrisi, E. Cavaliere, F. Banfi, G. Benetti, R. Raciti, L. Gavioli, A. Terrasi, Ag cluster beam deposition for TCO/Ag/TCO multilayer, Sol. Energy Mater. Sol. Cells. 199 (2019) 114–121, https://doi.org/10.1016/j.solmat.2019.04.025.

[5] S. Huang, Y. Liu, Y. Zhao, Z. Ren, C.F. Guo, Flexible Electronics: Stretchable Electrodes and Their Future, Adv. Funct. Mater. 29 (6) (2019) 1805924, https://doi.org/10.1002/adfm.v29.610.1002/adfm.201805924.

[6] Z. Li, H. Li, Z. Wu, M. Wang, J. Luo, H. Torun, PingAn Hu, C. Yang, M. Grundmann, X. Liu, YongQing Fu, Advances in designs and mechanisms of semiconducting metal oxide nanostructures for high-precision gas sensors operated at room temperature, Mater. Horiz. 6 (3) (2019) 470–506, https://doi.org/10.1039/C8MH01365A.

[7] E. Cavaliere, S. De Cesari, G. Landini, E. Riccobono, L. Pallecchi, G.M. Rossolini, L. Gavioli, Highly bactericidal Ag nanoparticle films obtained by cluster beam deposition, Nanomedicine Nanotechnol, Biol. Med. 11 (6) (2015) 1417–1423, https://doi.org/10.1016/j.nano.2015.02.023.

[8] G. Benetti, E. Cavaliere, A. Canteri, G. Landini, G.M. Rossolini, L. Pallecchi, M. Chiodi, M.J. Van Bael, N. Winckelmans, S. Bals, L. Gavioli, Direct synthesis of antimicrobial coatings based on tailored bi-elemental nanoparticles, APL Mater. 5 (3) (2017) 036105, https://doi.org/10.1063/1.4978772.

[9] G. Benetti, E. Cavaliere, R. Brescia, S. Salassi, R. Ferrando, A. Vantomme, L. Pallecchi, S. Pollini, S. Boncompagni, B. Fortuni, M.J. Van Bael, F. Banfi, L. Gavioli, Tailored Ag–Cu–Mg multielemental nanoparticles for wide-spectrum antibacterial coating, Nanoscale. 11 (4) (2019) 1626–1635, https://doi.org/10.1039/C8NR08375D.

[10] K.M. McPeak, S.V. Jayanti, S.J.P. Kress, S. Meyer, S. Iotti, A. Rossinelli, D. J. Norris, Plasmonic Films Can Easily Be Better: Rules and Recipes, ACS Photonics 2 (3) (2015) 326–333, https://doi.org/10.1021/ph5004237.

[11] A.S. Baburin, A.I. Ivanov, E.S. Lotkov, O.S. Sorokina, I.A. Boginskaya, E. V. Sergeev, K.A. Buzaverov, T.G. Konstantinova, D.O. Moskalev, Z. Issabayeva, I. A. Ryzhikov, I.A. Rodionov, Epitaxial Silver Films Morphology and Optical Properties Evolution over Two Years, Coatings. 10 (2020) 911, https://doi.org/10.3390/coatings10100911.

[12] M. Zhou, Y.-P. Li, S. Zhou, D.-Q. Liu, Optical Properties and Surface Morphology of Thin Silver Films Deposited by Thermal Evaporation*, Chin. Phys. Lett. 32 (7) (2015) 077802, https://doi.org/10.1088/0256-307X/32/7/077802.

[13] J. Gong, R. Dai, Z. Wang, Z. Zhang, Thickness Dispersion of Surface Plasmon of Ag Nano-thin Films: Determination by Ellipsometry Iterated with Transmittance Method, Sci. Rep. 5 (2015) 9279, https://doi.org/10.1038/srep09279.

[14] J.A. Sánchez-Gil, J.V. García-Ramos, E.R. Méndez, Electromagnetic mechanism in surface-enhanced Raman scattering from Gaussian-correlated randomly rough metal substrates, Opt. Express. 10 (17) (2002), 879, https://doi.org/10.1364/OE.10.00087910.1364/OE.10.000879.m001.

[15] R. Gupta, M.J. Dyer, W.A. Weimer, Preparation and characterization of surface plasmon resonance tunable gold and silver films, J. Appl. Phys. 92 (9) (2002) 5264–5271, https://doi.org/10.1063/1.1511275.

[16] W.A. Weimer, M.J. Dyer, Tunable surface plasmon resonance silver films, Appl. Phys. Lett. 79 (19) (2001) 3164–3166, https://doi.org/10.1063/1.1416473.

[17] D.G. Gromov, E.A. Lebedev, A.I. Savitskiy, A.Y. Trifonov, V.V. Rubcov, N. I. Borgardt, Y.S. Grishina, Investigation of condensation of small portions of Ag at thermal evaporation in vacuum, J. Phys. Conf. Ser. 643 (2015) 012014, https://doi.org/10.1088/1742-6596/643/1/012014.

[18] S.K. Sharma, S.U.M. Rao, N. Kumar, Hillock formation and agglomeration in silver films prepared by thermal evaporation, Thin Solid Films 142 (1) (1986) L95–L98, https://doi.org/10.1016/0040-6090(86)90311-1.

[19] K. Khurana, N. Rathee, N. Jaggi, Deposition of uniform plasmonic Ag nanoparticles by in-situ substrate heating using thermal evaporator, AIP Conf. Proc. 2220 (2020), 090006, https://doi.org/10.1063/5.0001691.

[20] H.U. Yang, J. D'Archangel, M.L. Sundheimer, E. Tucker, G.D. Boreman, M. B. Raschke, Optical dielectric function of silver, Phys. Rev. B. 91 (2015), 235137, https://doi.org/10.1103/PhysRevB.91.235137.

[21] J. Choi, F. Cheng, J.W. Cleary, L. Sun, C.K. Dass, J.R. Hendrickson, C.-Y. Wang, S. Gwo, C.-K. Shih, X. Li, Optical dielectric constants of single crystalline silver films in the long wavelength range, Opt. Mater. Express. 10 (2) (2020) 693, https://doi.org/10.1364/OME.385723.

[22] B.K. Kim, S.Y. Lee, Optimized Design of SiInZnO/Ag/SiInZnO Transparent Conductive Electrode by Using Optical Admittance Simulation, Trans. Electr. Electron. Mater. 21 (3) (2020) 324–328, https://doi.org/10.1007/s42341-020-00178-z.

[23] P.B. Johnson, R.W. Christy, Optical Constants of the Noble Metals, Phys. Rev. B. 6 (12) (1972) 4370–4379, https://doi.org/10.1103/PhysRevB.6.4370.

[24] J.E. Nestell, R.W. Christy, Derivation of Optical Constants of Metals from Thin-Film Measurements at Oblique Incidence, Appl. Opt. 11 (1972) 643–651, https://doi.org/10.1364/AO.11.000643.

[25] W.P. Chen, J.M. Chen, Use of surface plasma waves for determination of the thickness and optical constants of thin metallic films, JOSA. 71 (1981) 189–191, https://doi.org/10.1364/JOSA.71.000189.

[26] E. Fontana, Thickness optimization of metal films for the development of surface-plasmon-based sensors for nonabsorbing media, Appl. Opt. 45 (2006) 7632–7642, https://doi.org/10.1364/AO.45.007632.

[27] Y. Pan, Y. Fan, J. Niu, Optical properties of ultra-thin silver films deposited by thermal evaporation and its application in optical filters, Infrared Phys. Technol. 104 (2020), 103123, https://doi.org/10.1016/j.infrared.2019.103123.

[28] M.N.M.N. Perera, D. Schmidt, W.E.K. Gibbs, S. Juodkazis, P.R. Stoddart, Influence of the dielectric substrate on the effective optical constants of silver plasmonic films, Appl. Opt. 58 (22) (2019) 6038, https://doi.org/10.1364/AO.58.006038.

[29] G. Rizzi, G. Benetti, C. Giannetti, L. Gavioli, F. Banfi, Analytical model of the acoustic response of nanogranular films adhering to a substrate, Phys. Rev. B. 104 (2021), 035416, https://doi.org/10.1103/PhysRevB.104.035416.

[30] N. Bontempi, E. Cavaliere, V. Cappello, P. Pingue, L. Gavioli, Ag@TiO$_2$ nanogranular films by gas phase synthesis as hybrid SERS platforms, Phys. Chem. Chem. Phys. 21 (45) (2019) 25090–25097, https://doi.org/10.1039/C9CP03998H.

[31] T.C. Choy, Effective Medium Theory: Principles and Applications, Oxford University Press, 2015.

[32] D. Lehmann, F. Seidel, D. Zahn, Thin films with high surface roughness: Thickness and dielectric function analysis using spectroscopic ellipsometry, SpringerPlus. 3 (2014) 82, https://doi.org/10.1186/2193-1801-3-82.

[33] D.E. Aspnes, Optical properties of thin films, Thin Solid Films 89 (3) (1982) 249–262, https://doi.org/10.1016/0040-6090(82)90590-9.

[34] B.K. Juluri, Y.B. Zheng, D. Ahmed, L. Jensen, T.J. Huang, Effects of Geometry and Composition on Charge-Induced Plasmonic Shifts in Gold Nanoparticles, J. Phys. Chem. C. 112 (19) (2008) 7309–7317, https://doi.org/10.1021/jp077346h10.1021/jp077346h.s002.

[35] E. Cavaliere, G. Benetti, M. Van Bael, N. Winckelmans, S. Bals, L. Gavioli, Exploring the Optical and Morphological Properties of Ag and Ag/TiO2 Nanocomposites Grown by Supersonic Cluster Beam Deposition, Nanomaterials. 7 (2017) 442, https://doi.org/10.3390/nano7120442.

[36] C. Noguez, Surface Plasmons on Metal Nanoparticles: The Influence of Shape and Physical Environment, J. Phys. Chem. C. 111 (2007) 3806–3819, https://doi.org/10.1021/jp066539m.

[37] F. Bisio, M. Palombo, M. Prato, O. Cavalleri, E. Barborini, S. Vinati, M. Franchi, L. Mattera, M. Canepa, Optical properties of cluster-assembled nanoporous gold films, Phys. Rev. B. 80 (2009), 205428, https://doi.org/10.1103/PhysRevB.80.205428.

[38] H. Monard, F. Sabary, Optical properties of silver, gold and aluminum ultra-thin granular films evaporated on oxidized aluminum, Thin Solid Films 310 (1-2) (1997) 265–273, https://doi.org/10.1016/S0040-6090(97)00331-3.

[39] P. Gnanadurai, N. Sivaraja, N. Soundrarajan, C. Vijayan, Influence of annealing on the optical properties of vacuum deposited silver thin films, AIP Conf. Proc. 1665 (2015), 080071, https://doi.org/10.1063/1.4917975.

[40] K. Aslan, S.N. Malyn, Y. Zhang, C.D. Geddes, Conversion of just-continuous metallic films to large particulate substrates for metal-enhanced fluorescence, J. Appl. Phys. 103 (8) (2008) 084307, https://doi.org/10.1063/1.2905319.

[41] M.M. Rahman, N. Hattori, Y. Nakagawa, X.u. Lin, S. Yagai, M. Sakai, K. Kudo, K. Yamamoto, Preparation and characterization of silver nanoparticles on localized surface plasmon-enhanced optical absorption, Jpn. J. Appl. Phys. 53 (11S) (2014), 11RE01, https://doi.org/10.7567/JJAP.53.11RE01.

[42] S. Yamaguchi, Theory of the Optical Properties of Very Thin Inhomogeneous Films, J. Phys. Soc. Jpn. 17 (1) (1962) 184–193, https://doi.org/10.1143/JPSJ.17.184.

[43] J. Toudert, D. Babonneau, L. Simonot, S. Camelio, T. Girardeau, Quantitative modelling of the surface plasmon resonances of metal nanoclusters sandwiched between dielectric layers: the influence of nanocluster size, shape and organization, Nanotechnology. 19 (12) (2008), 125709, https://doi.org/10.1088/0957-4484/19/12/125709.

[44] V.V. Truong, G.D. Scott, Optical properties of aggregated noble metal films*, JOSA. 67 (1977) 502–510, https://doi.org/10.1364/JOSA.67.000502.

[45] A. Mejdoubi, C. Brosseau, Finite-Element Simulation of the Depolarization Factor of Arbitrarily Shaped Inclusions, Phys. Rev. E Stat. Nonlin. Soft Matter. Phys. 44 (6) (2008) 1142–1145, https://doi.org/10.1109/TMAG.2007.916492.

[46] K.-P. Chen, V.P. Drachev, J.D. Borneman, A.V. Kildishev, V.M. Shalaev, Drude Relaxation Rate in Grained Gold Nanoantennas, Nano Lett. 10 (3) (2010) 916–922, https://doi.org/10.1021/nl9037246.

[47] S. Norrman, T. Andersson, C.G. Granqvist, O. Hunderi, Optical properties of discontinuous gold films, Phys. Rev. B. 18 (2) (1978) 674–695, https://doi.org/10.1103/PhysRevB.18.674.

[48] E. Anno, R. Hoshino, Size Effect on the Width of Plasma Resonance Absorption of Silver Island Films, J. Phys. Soc. Jpn. 51 (4) (1982) 1185–1192, https://doi.org/10.1143/JPSJ.51.1185.

[49] A. Kawabata, R. Kubo, Electronic Properties of Fine Metallic Particles. II. Plasma Resonance Absorption, J. Phys. Soc. Jpn. 21 (9) (1966) 1765–1772, https://doi.org/10.1143/JPSJ.21.1765.

[50] U. Kreibig, L. Genzel, Optical absorption of small metallic particles, Surf. Sci. 156 (1985) 678–700, https://doi.org/10.1016/0039-6028(85)90239-0.

[51] E.A. Coronado, G.C. Schatz, Surface plasmon broadening for arbitrary shape nanoparticles: A geometrical probability approach, J. Chem. Phys. 119 (7) (2003) 3926–3934, https://doi.org/10.1063/1.1587686.

[52] G. Torrisi, I. Crupi, S. Mirabella, A. Terrasi, Robustness and electrical reliability of AZO/Ag/AZO thin film after bending stress, Sol. Energy Mater Sol. Cells 165 (2017) 88–93, https://doi.org/10.1016/j.solmat.2017.02.037.